Theory and Design of Phononic Crystals for Unreleased CMOS-MEMS Resonant Body Transistors

Bichoy Bahr, *Student Member, IEEE*, Radhika Marathe, *Student Member, IEEE*, and Dana Weinstein, *Member, IEEE*

Abstract*— Resonant body transistors (RBTs) are solid state, actively sensed microelectromechanical systems (MEMS) resonators that can be implemented in commercial CMOS technologies. With small footprint, high-Q, and scalability to gigahertz frequencies, they form basic building blocks for radio frequency (RF) front-ends and timing applications. Toward the goal of seamless CMOS integration, this paper presents the design and implementation of phononic crystals (PnCs) in the back-end-of-line (BEOL) of commercial CMOS technologies with bandgaps in the gigahertz frequencies to be used for enhanced acoustical confinement in CMOS-RBTs. Lithographically defined PnC dimensions allow for bandgap engineering, providing flexibility in resonator design, and allowing for multiple frequencies on a single chip. The theoretical basis for analyzing generic PnCs is presented, with focus on the special case of implementing PnCs in CMOS BEOL layers. The effect of CMOS process variations on the performance of such PnCs is also considered. The analysis presented in this paper establishes a methodology for assessing different CMOS technologies for the integration of unreleased CMOS-MEMS resonators. This paper also discusses the importance of uniformity of the acoustical cavity in the nonresonant dimension and its effect on overall resonator performance. A PnC implementation in IBM 32-nm silicon on insulator (SOI) BEOL layers is demonstrated to achieve 85% fractional-bandgap ∼4.5-GHz frequency. With better energy confinement, the proposed CMOS-RBTs achieve a quality factor Q of 252, which corresponds to 8× improvement over the previous generation RBTs, which did not include PnCs. The presented devices have a footprint of 5 μm × 7 μm. This paper concludes with a discussion of the properties required of a CMOS technology for high performance RBT implementation. [2014-0364]

***Index Terms*— CMOS-microelectromechanical systems (MEMS), radio frequency (RF) MEMS, resonators, resonant body transistor (RBT), phononic crystals.**

I. Introduction

FREQUENCY sources and high quality filters are essential building blocks for both analog and digital electronics, and communication systems. They are becoming more and more ubiquitous every day with growing applications that require further reduction in size, weight and power consumption, driving toward unprecedented scaling and integration of frequency sources and filters. Integration of micro-electro-mechanical (MEM) resonators with CMOS have been studied extensively and several approaches have been proposed [1]–[3], with the most notable including MEMS-first, MEMS-last and CMOS-MEMS technologies. However, these techniques require extensive post-processing, and complicated protection techniques for various parts of the chip at different stages of the fabrication process. Furthermore, the resulting MEMS devices always have exposed moving surfaces, requiring hermetic sealing together with specialized and costly packaging to avoid device performance degradation with time and to shield them from the surrounding environment [4]–[6].

The authors have previously proposed and demonstrated a new class of CMOS-MEMS resonators at GHz-frequencies, that does not require any post-processing or special packaging [7]. These CMOS-MEMS resonators are truly solid-state devices without any exposed freely moving surfaces; they are completely embedded in the CMOS die to form a single solid entity. An acoustic resonance cavity is formed in the front-end-of-line (FEOL) layers of the CMOS die by localized confinement of acoustic vibrations. This work demonstrates the usage of phononic crystals (PnCs) implemented in back-end-of-line (BEOL) materials (Fig. 1) to significantly improve the confinement of acoustic vibrations,

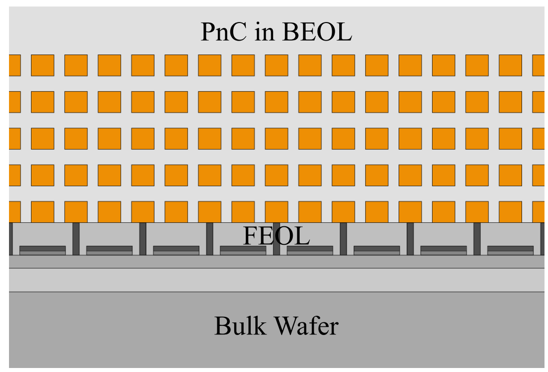

Fig. 1. Cross section of a phononic crystal (PnC) implemented as periodic metal stripes in the back-end-of-line (BEOL) of CMOS technology above the front-end-of-line (FEOL) and bulk silicon wafer.

Manuscript received December 2, 2014; revised March 3, 2015; accepted March 24, 2015. Date of publication April 27, 2015; date of current version September 29, 2015. This work was supported by the Defense Advanced Research Projects Agency through the Unconventional Processing of Signals for Intelligent Data Exploitation Program under Grant 12105-301702-DS. Subject Editor G. Piazza.

The authors are with the Department of Electrical Engineering and Computer Science, Massachusetts Institute of Technology, Cambridge, MA 02139 USA (e-mail: bichoy@mit.edu; marathe@mit.edu; dana@mtl.mit.edu).

Color versions of one or more of the figures in this paper are available online at http://ieeexplore.ieee.org.

Digital Object Identifier 10.1109/JMEMS.2015.2418789

increasing the quality factor of the resonators by an order of magnitude.

PnCs are periodic composite structures that allow the control of propagation of elastic waves through them by virtue of their dispersion characteristics [8]–[15]. Bandgaps are a characteristic feature of a PnC's dispersion relation that prohibit elastic wave propagation in one or more directions. The ability to engineer such bandgaps by proper material and geometric selection makes PnCs very attractive for achieving acoustic confinement, a critical feature of high-Q mechanical resonator and filter design [11]–[14], [16]. Moreover, the lithographically defined PnC dimensions allow for flexibility in RBT design, enabling multiple frequencies on a single chip, as opposed to thickness mode film-bulk-acoustic-resonators (FBARs) [17] and solidly mounted resonators (SMR) [18].

When considering monolithically integrated MEMS resonators in CMOS, FET sensing becomes a natural choice to harness the high-quality, high-yield MOSFETs available in CMOS technologies. Active transistor sensing for MEMS resonators has been widely demonstrated over different technology platforms, including FETs [7], [19]–[21] and HEMT sensing [22]–[25]. Elastic wave stresses modulate carrier mobility and density in the FET channel by virtue of piezoresistivity and dielectric thickness modulation, respectively [7]. This creates a small signal AC current in the read-out circuit, when the FET is biased properly. Moreover, active FET sensing has been proven to have superior noise performance over piezoresistive sensing. Since the electromechanical transconductance efficiency g_{em}/I_{DS} is enhanced for smaller dimensions, sensing transducers can be scaled to the technology's minimum dimensions limits, significantly reducing the resonator footprint. Finally, active FET sensing is less sensitive to direct capacitive feedthrough, enabling simple detection schemes at higher operational frequencies than possible with passive sensing mechanisms.

In this paper, the design of CMOS-MEMS RBTs based on PnCs for acoustic confinement in commercial CMOS technologies is presented. The paper is organized as follows: Section II introduces a theoretical basis for the analysis of phononic crystals. The special case of possible CMOS implementations is also presented. A comparison of the performance of PnC designs in different commercial CMOS technologies follows this discussion. Section III addresses the proposed RBT implementation based on phononic crystals, along with the requirements imposed on cavity uniformity. Section IV presents simulation and measurement results for the proposed RBTs, along with additional measurements comparing the effects of cavity uniformity on RBT performance. Finally, the conclusion is presented in section V.

II. Phononic Crystals in CMOS

A. Phononic Crystal Theory

The linear elastic behavior of solid materials is governed by Hooke's law [26]:

$$T = c : S \tag{1}$$

where T and S are the second rank stress and strain tensors, respectively and $c = c(\vec{r})$ is a fourth rank tensor representing the stiffness coefficients of the material. With the absence of internal torques in the material, the number of independent parameters in (1) is significantly reduced by virtue of multiple symmetries. In this case, using Voigt notation [26] is more convenient, as T and S in (1) reduce to column vectors, whereas c reduces to a 6×6 matrix:

$$T = [T_{xx} \quad T_{yy} \quad T_{zz} \quad T_{zy} \quad T_{xz} \quad T_{xy}]^{\mathrm{T}} \tag{2a}$$

$$S = [S_{xx} \quad S_{yy} \quad S_{zz} \quad S_{zy} \quad S_{xz} \quad S_{xy}]^{\mathrm{T}} \tag{2b}$$

$$T_I = C_{IJ} S_J \quad \forall I, J \in \{1, 2, \cdots, 6\} \tag{2c}$$

In this notation, the kinematic and dynamic behavior can be described as [26]:

$$\frac{\partial S}{\partial t} = \nabla_s \vec{v}; \quad \frac{\partial}{\partial t}(\rho \vec{v}) = \nabla \cdot T = \nabla \cdot (c : S) \tag{3}$$

where $\vec{v} = \vec{v}(\vec{r})$ is the velocity vector field (3×1 column vector), $\rho = \rho(\vec{r})$ is the material density and the symmetric divergence $\nabla\cdot$ and gradient ∇_s are defined as:

$$\nabla \cdot = \begin{bmatrix} \partial_x & 0 & 0 & 0 & \partial_z & \partial_y \\ 0 & \partial_y & 0 & \partial_z & 0 & \partial_x \\ 0 & 0 & \partial_z & \partial_y & \partial_x & 0 \end{bmatrix}; \quad \nabla_s = (\nabla \cdot)^{\mathrm{T}} \tag{4}$$

Assuimg a harmonic time dependence $e^{i\omega t}$, combining the equations in (3) yields the elastic wave equations in solids which can be properly formulated as:

$$-\nabla \cdot (c : \nabla_s \vec{u}) = \omega^2 \rho \vec{u} \tag{5}$$

where $\vec{u} = \vec{u}(\vec{r})$ is the displacement field. The wave equation for the velocity field $\vec{v}$ is the same as (5), since $\vec{v} = i\omega\vec{u}$. Equation (5) is a generalized Hermitian eigenproblem on the form:

$$\hat{A}\vec{u} = \lambda \hat{B}\vec{u} \tag{6}$$

with $\hat{A} = -\nabla \cdot c : \nabla_s$, $\hat{B} = \rho(\vec{r})$ and $\lambda = \omega^2$, with $\hat{A}$ and $\hat{B}$ Hermitian operators for the inner product defined as:

$$\langle \vec{\mu} | \vec{\nu} \rangle = \int_\Omega d\Omega\, \vec{\mu}^* \cdot \vec{\nu} \tag{7}$$

where * denotes complex conjugation. A proof of the hermiticity of $\hat{A}$ is found in [27]. The solutions of (6) form a complete and orthogonal set of bases for a Hilbert space $\mathcal{H}$ over $\mathbb{C}$, with the inner product $\langle \mu | \nu \rangle_{\hat{B}}$ defined as:

$$\langle \vec{\mu} | \vec{\nu} \rangle_{\hat{B}} = \int_\Omega d\Omega\, \vec{\mu}^* \cdot \hat{B}\vec{\nu} \tag{8}$$

The inner product of the velocity field $\langle \vec{v} | \vec{v} \rangle_{\hat{B}}$ is directly proportional to the stored kinetic energy. The orthogonality of modes implies that two different eigenmodes $\vec{v}_1$ and $\vec{v}_2$ will have $\langle \vec{v}_1 | \vec{v}_2 \rangle_{\hat{B}} = 0$. For non-degenerate eigenmodes, this physically signifies that the energy of each mode is preserved and different modes are not allowed to exchange energy between them. For degenerate eigenmodes, it is always possible to find linear combinations thereof that satisfy orthogonality under (8) [28].

The structure may possess a certain symmetry (e.g. mirror or translational symmetry) to be associated with an operator $\hat{O}$.

Applying the symmetry operator $\hat{O}$ before or after the operator $\hat{A}$ must yield the same result, thus for the structure to be symmetric under $\hat{O}$ we must have:

$$\hat{A} = \hat{O}^{-1}\hat{A}\hat{O} \Rightarrow \hat{O}\hat{A} - \hat{A}\hat{O} = 0 \Rightarrow [\hat{O}, \hat{A}] = 0 \tag{9}$$

where $[,]$ denotes the commutator bracket. Since symmetry operators are required to commute with $\hat{A}$ and $\hat{B}$ of (6), they share the same eigenmodes with $\hat{A}$ and $\hat{B}$. Symmetry operations are also required to preserve the stored kinetic and strain energy, which are proportional to the inner products $\langle v|v\rangle_{\hat{B}}$ and $\langle S|T\rangle$, respectively [26]. This dictates that symmetry operators must be unitary (or anti-unitary), i.e. $\hat{O}^{\dagger}\hat{O} = I$, and hence $\hat{O}^{\dagger} = \hat{O}^{-1}$.

Since PnCs are periodic structures, we are primarily concerned with translational symmetry. A translation operator $\hat{T}(\vec{d})$ may be defined as:

$$\hat{T}(\vec{d})\vec{u}(\vec{r}) = \vec{u}(\vec{r} - \vec{d}) \tag{10}$$

In addition to unitarity, this operator must satisfy the composition property:

$$\hat{T}(\vec{a} + \vec{b}) = \hat{T}(\vec{a})\hat{T}(\vec{b}) \tag{11}$$

It is clear that a plane wave of the form $\vec{u}_{\circ}e^{i\vec{k}\cdot\vec{r}}$ with wave vector $\vec{k}$ is an eigenfunction of $\hat{T}(\vec{d})$:

$$\hat{T}(\vec{d})\vec{u}_{\circ}e^{i\vec{k}\cdot\vec{r}} = \vec{u}_{\circ}e^{i\vec{k}\cdot(\vec{r}-\vec{d})} = e^{-i\vec{k}\cdot\vec{d}}\vec{u}_{\circ}e^{i\vec{k}\cdot\vec{r}} \tag{12}$$

with eigenvalue $e^{-i\vec{k}\cdot\vec{d}}$. The unitarity and composition properties of $\hat{T}(\vec{d})$ are easily verified in this case. Thus, plane waves are solutions of (5) in homogeneous media with continuous translational symmetry. And since $\hat{A}$ and $\hat{T}(\vec{d})$ share the same eigenmodes (as they commute), we can label the eigenmodes with the eigenvalues of the latter, or simply with their corresponding value of $\vec{k}$. For the case of plane waves, they have a linear dispersion relation such that $\omega = c|\vec{k}|$, where c is the speed of sound for the given wave type, being longitudinal (P-wave) or shear (S-wave).

PnCs on the other hand are characterized by discrete translational symmetry. Consider the periodic PnC structure to be generated by translating a *unit cell* along the lattice vector $\vec{R} = l\,\vec{a}_1 + m\,\vec{a}_2 + n\,\vec{a}_3$, where $\vec{a}_i$ are the primitive lattice vectors and (l, m, n) are integers. A translation operator $\hat{T}(\vec{d} + \vec{R})$ applied to a plane wave solution yields:

$$\hat{T}(\vec{d} + \vec{R})e^{i\vec{k}\cdot\vec{r}} = e^{-i\vec{k}\cdot\vec{R}}e^{-i\vec{k}\cdot\vec{d}}e^{i\vec{k}\cdot\vec{r}} \tag{13}$$

and hence solutions with $\vec{k}\cdot\vec{R} = 2\pi N$ with $N \in \mathbb{Z}$ are in fact degenerate and share the same eigenvalue of $e^{-i\vec{k}\cdot\vec{d}}$. Thus, $\vec{k}$ can be assumed to obtain its values from a *reciprocal lattice*, with primitive lattice vectors $\vec{b}_i$ defined as:

$$\vec{b}_1 = \frac{2\pi\,\vec{a}_2 \times \vec{a}_3}{\vec{a}_1 \cdot \vec{a}_2 \times \vec{a}_3};\quad \vec{b}_2 = \frac{2\pi\,\vec{a}_1 \times \vec{a}_3}{\vec{a}_1 \cdot \vec{a}_2 \times \vec{a}_3};\quad \vec{b}_3 = \frac{2\pi\,\vec{a}_1 \times \vec{a}_2}{\vec{a}_1 \cdot \vec{a}_2 \times \vec{a}_3} \tag{14}$$

and reciprocal lattice vectors $\vec{G} = l'\,\vec{b}_1 + m'\,\vec{b}_2 + n'\,\vec{b}_3$, such that $\vec{G}\cdot\vec{R} = 2\pi N$. This makes the set of solutions corresponding to $\vec{k} + \vec{G}$ a denumerably infinite set of degenerate solutions for all $l', m', n' \in \mathbb{Z}$. Since a linear combination of the degenerate solutions is itself a solution, one can form the linear sum:

$$\begin{aligned}\vec{u}(\vec{r}) &= \sum_G c_G e^{i\vec{k}\cdot\vec{r}}e^{i\vec{G}.\vec{r}} = e^{i\vec{k}\cdot\vec{r}}\sum_G c_G e^{i\vec{G}.\vec{r}}\\ &= e^{i\vec{k}\cdot\vec{r}}\vec{u}_k(\vec{r})\end{aligned} \tag{15}$$

where $\vec{u}_k(\vec{r})$ is a periodic function on the PnC lattice (as recognized from its Fourier series expansion above) such that $\vec{u}_k(\vec{r}+\vec{R}) = \vec{u}_k(\vec{r})$. This is *Bloch theorem* for waves in periodic structures and forms the basis of PnC theory [28], [29]. The *first Brillouin Zone* refers to the region in the reciprocal lattice that is closest to $\vec{k} = 0$ and contains distinct modes that can't be obtained from one another by applying a $\vec{G}$ shift to $\vec{k}$.

In addition to translational symmetry, PnCs may also possess rotational symmetry, defined by an operator $\hat{\mathcal{R}}(\hat{n}, \theta)$ that rotates vectors by angle θ around axis $\hat{n}$. The corresponding operator $\hat{O}_{\mathcal{R}}$ to rotate a vector field $\vec{u}(\vec{r})$ is defined as:

$$\hat{O}_{\mathcal{R}}\vec{u}(\vec{r}) = \hat{\mathcal{R}}\vec{u}(\hat{\mathcal{R}}^{-1}\vec{r}) \tag{16}$$

With a given rotational symmetry, the unitary rotation operator $\hat{O}_{\mathcal{R}}$ commutes with $\hat{A}$ and $\hat{B}$ from (6), such that:

$$\begin{aligned}\hat{A}(\hat{O}_{\mathcal{R}}\vec{u}(\vec{r})) &= \hat{O}_{\mathcal{R}}(\hat{A}\vec{u}(\vec{r})) = \hat{O}_{\mathcal{R}}(\omega^2(\vec{k})\hat{B}\vec{u}(\vec{r}))\\ &= \omega^2(\vec{k})\hat{B}(\hat{O}_{\mathcal{R}}\vec{u}(\vec{r}))\end{aligned} \tag{17}$$

which indicates that $\hat{O}_{\mathcal{R}}\vec{u}(\vec{r})$ are eigenmodes with the same frequency $\omega^2(\vec{k})$ as $\vec{u}(\vec{r})$. As for the translation operator $\hat{T}(\vec{R})$ we have [28]:

$$\begin{aligned}\hat{T}(\vec{R})(\hat{O}_{\mathcal{R}}\vec{u}(\vec{r})) &= \hat{O}_{\mathcal{R}}(\hat{T}(\hat{\mathcal{R}}^{-1}\vec{R})\vec{u}(\vec{r}))\\ &= \hat{O}_{\mathcal{R}}(e^{-i\vec{k}\cdot\hat{\mathcal{R}}^{-1}\vec{R}}\vec{u}(\vec{r}))\\ &= e^{-i(\hat{\mathcal{R}}\vec{k})\cdot\vec{R}}\hat{O}_{\mathcal{R}}\vec{u}(\vec{r})\end{aligned} \tag{18}$$

where we have used $\vec{k}\cdot(\hat{\mathcal{R}}^{-1}\vec{R}) = (\hat{\mathcal{R}}\vec{k})\cdot\vec{R}$ from the unitarity of $\hat{\mathcal{R}}$. Thus, the eigenmode $\hat{O}_{\mathcal{R}}\vec{u}(\vec{r})$ has the same frequency $\omega^2(\vec{k})$ as $\vec{u}(\vec{r})$, but it is also associated with the reciprocal lattice vector $\hat{\mathcal{R}}\vec{k}$, so that $\omega^2(\hat{\mathcal{R}}\vec{k}) = \omega^2(\vec{k})$. Thus, the reciprocal lattice possesses the same symmetry as the PnC lattice. The same is true for all the *point group* symmetries (rotation, reflection and inversion) of the lattice [28]. Moreover, since $\hat{A}$ and $\hat{B}$ are Hermitian, conjugation of (6) leads to time reversal symmetry, and hence $\omega(\vec{k}) = \omega(-\vec{k})$. By virtue of the different symmetries, a subset of the first Brillouin Zone called the *Irreducible Brillouin Zone* (IBZ) is sufficient to generate the entire reciprocal lattice. The extrema of the dispersion relation $\omega(\vec{k})$ will usually occur at the edges of the IBZ [28], and thus for all practical purposes, it is sufficient to solely study the boundaries of the IBZ to fully characterize the phononic crystal bandgaps.

It is also important to consider the effects of coordinate and material transformations on the PnC dispersion relation. Consider a coordinate scaling of the form of a linear mapping $\vec{r} \mapsto s\vec{r}$ for some $s \in \mathbb{R}^+$. Using $\vec{r}\,' = s\vec{r}$ and $\nabla' = \nabla/s$, the master equation (5) becomes:

$$-\nabla' \cdot c'(\vec{r}\,') : \nabla_s'\vec{u}(\frac{\vec{r}\,'}{s}) = \left(\frac{\omega}{s}\right)^2 \rho'(\vec{r}\,')\vec{u}(\frac{\vec{r}\,'}{s}) \tag{19}$$

where $c'(\vec{r}\,') = c(\vec{r}\,'/s)$ and $\rho'(\vec{r}\,') = \rho(\vec{r}\,'/s)$. Thus, uniform coordinate scaling results in an inversely proportional scaling

TABLE I
MECHANICAL PROPERTIES FOR POPULAR MATERIALS IN COMMERCIAL CMOS TECHNOLOGIES

Material	ρ (kg/m^3)	c_{11} (GPa)	Z_{11} $(MRayl)$	c_{44} (GPa)	Z_{44} $(MRayl)$
Si< 100 >	2329	194.3	21.2	79.5	13.6
SiO_2	2200	75.2	12.9	29.9	8.1
SiCOH	1060	3.96	2.05	1.32	1.18
TEOS	2160	49.4	10.3	19.7	6.5
Tungsten	17600	525.5	96.2	160.5	53.1
Copper	8700	176.5	39.1	40.7	18.8
Aluminum	2735	111.1	17.4	28.9	8.9

of the frequency $\omega \mapsto \omega/s$. Moreover, scaling of material properties $c \mapsto s^2 c$ or $\rho \mapsto \rho/s^2$, will result in a similar scaling for the frequency $\omega \mapsto \omega/s$. This very simple conclusion has far reaching and important results. It allows a designer to engineer the dispersion characteristics $\omega(\vec{k})$ of a PnC by scaling appropriate dimensions. Moreover, it helps build intuition about perturbations in dimensions or material properties which proves to be very useful in characterizing fabrication variations and structural non-idealities.

B. CMOS PnC Implementations

The width of the PnC bandgap depends on the acoustic impedance mismatch, among other factors [8], [15], [28]. The authors have previously demonstrated in [11] that the BEOL layers of CMOS technologies usually have several materials with large acoustic impedance contrast that can be used to create wide-bandgap PnCs. Table I lists common CMOS BEOL materials along with their acoustic impedances. Copper metallization in low-κ SiCOH dielectric background as well as tungsten in SiO_2 are notable examples, with impedance contrast ratios on the order of 19$\times$ and 7$\times$, respectively. The ability to create wide bandgap PnCs in solid-state CMOS makes them ideal for achieving high acoustic confinement in unreleased CMOS RBTs.

Commercial CMOS technologies usually have a strict Design Rules Check (DRC), that is imposed to guarantee the manufacturability of the different designs. DRC rules include specifications for different metal widths, separations and even restrictions on maximum and minimum filling densities. The designer only has control over lateral dimensions, whereas the vertical dimensions are fixed process parameters. This imposes many restrictions on the feasible structures and dimensions of a PnC implemented in CMOS. The simplest 2D PnC design in CMOS consists of parallel and periodic rectangular metal lines, formed from different BEOL layers. From a technology and manufacturability point of view, this structure is highly favorable since it is very similar to parallel bus connections. This structure is usually simple enough to design according to the DRC rules of the CMOS process.

A schematic cross section of the abovementioned structure in IBM 32 nm silicon on insulator (SOI) technology [30] is shown in Fig. 1. The copper metal stripes have a width of 165 nm and a spacing of 85 nm, both in x-direction. The corresponding unit cell as well as the IBZ are shown in Fig. 2(a).

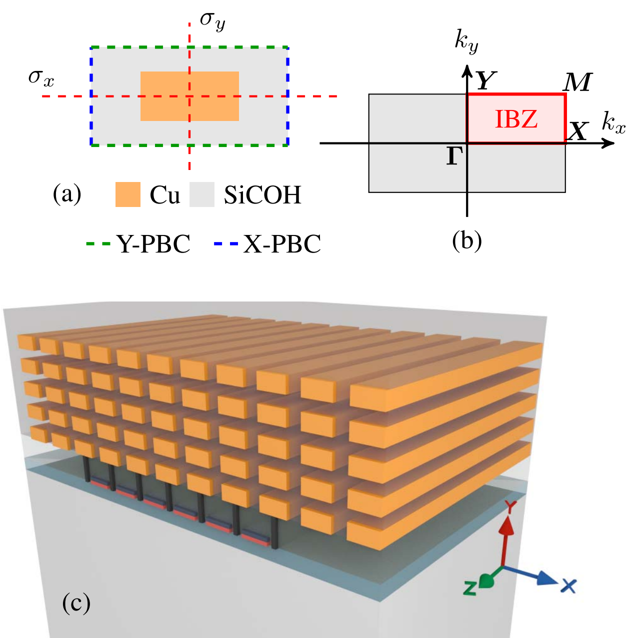

Fig. 2. (a) Unit cell for a PnC implemented in IBM 32 nm SOI technology BEOL, showing the mirror axes σ_x and σ_y. Blue and green dashed lines indicate the periodic boundary conditions applied in FEM simulation. (b) First Brillouin Zone and IBZ of the reciprocal lattice for the unit cell of (a). (c) 3D view of the full PnC on top of an RBT.

The unit cell has two mirror symmetries, namely, σ_x and σ_y, which, along with time reversal symmetry, reduce the first Brillouin Zone to the rectangular IBZ shown in Fig. 2(b). The IBZ doesn't have the familiar triangular shape (associated with square unit cells), since its unit cell lacks the 90° (C_{4v}) rotational symmetry. This will usually be the general case for most CMOS technologies. Assuming the unit cell has height b and width a, the primitive lattice vectors as well as the reciprocal lattice vectors are given by:

$$\vec{a}_1 = a\hat{x}, \quad \vec{a}_1 = b\hat{y}; \quad \vec{b}_1 = \frac{2\pi}{a}\hat{x}, \quad \vec{b}_2 = \frac{2\pi}{b}\hat{y} \tag{20}$$

As the extrema of the dispersion relation will occur at the edges of the IBZ, thus for all practical purposes, it is sufficient to consider wave vectors $\vec{k}$ in the sequence:

$$\frac{k_x a}{\pi} : 0 \to 1 \to 1 \to 0 \tag{21a}$$

$$\frac{k_y b}{\pi} : 0 \to 0 \to 1 \to 0 \tag{21b}$$

To find $\omega(\vec{k})$ of the PnC, numerical simulation is required. For this purpose, finite element modeling (FEM) is preferred for its accuracy, good convergence and efficiency [10]. 2D FEM simulation with plane strain approximation is used to find the eigenfrequencies of the PnC unit cell of Fig. 2(a). COMSOL Multiphysics solid mechanics module is used for such simulation [31]. Floquet periodic boundary conditions (PBC) are set at the opposite edges of the 2D unit cell in x and y directions, as shown in Fig. 2(a). The PBC spatial periodicity vector is set to $\vec{k}$. Eigenfrequency analysis is carried out with $\vec{k}$ as a parameter, which is swept over

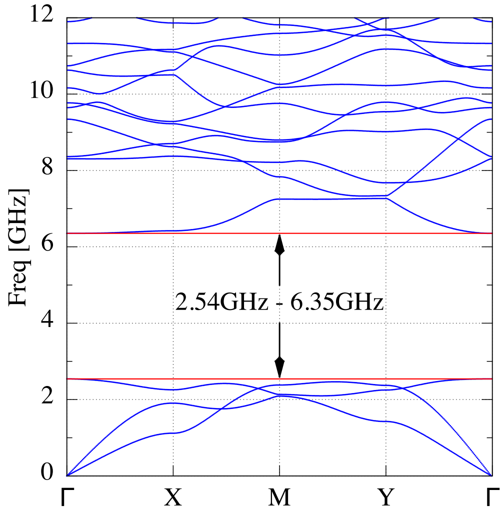

Fig. 3. Dispersion relation for the PnC of Fig. 2 implemented in IBM 32 nm SOI technology, showing a bandgap of 3.81 GHz (2.54 GHz - 6.35 GHz).

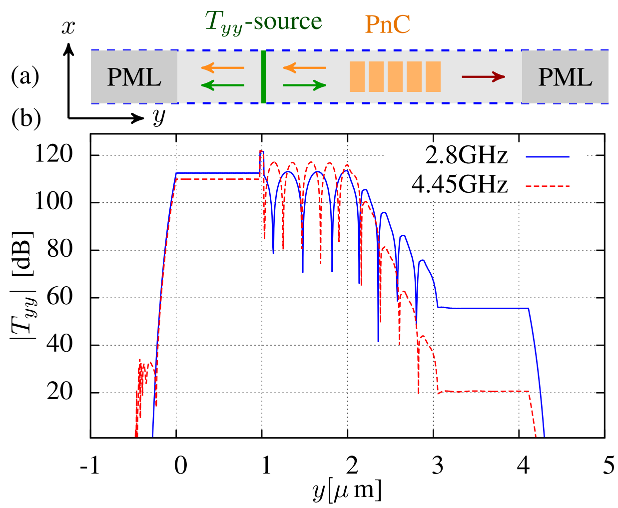

Fig. 4. (a) FEM model for 5 layers of the PnC of Fig. 2 (plotted horizontally), (b) Magnitude of the stress field $|T_{yy}|$ along the structure, showing: standing waves between the source and PnC, exponentially decaying waves in the PnC as well as transmitted waves after the PnC.

the edges of the IBZ as in (21). The resulting dispersion relation for a PnC with typical dimensions in IBM 32 nm SOI is shown in Fig. 3. The dispersion relation clearly shows a complete, 85% fractional bandgap spanning 3.8GHz, centered at 4.45GHz (2.54GHz-6.35GHz), in which no waves are allowed to propagate in x or y directions.

Although such PnC implementation is limited to the first five metal layers available in the IBM technology, it achieves high reflectivity owing to the large impedance contrast between SiCOH and Cu. This is verified through FEM simulation of a vertical section (a complete period in the x-direction) from the PnC as shown in Fig. 4(a) (the section is rotated horizontally for plotting convenience, such that the silicon substrate is on the left and the top of the CMOS stack is on the right). Periodic boundary conditions are enforced in the x-direction. A 1 MPa y-stress (T_{yy}) is applied from the wafer side, launching waves towards the PnC and the wafer bulk, where the latter is modeled as a perfectly matched layer (PML) [32]. Magnitude of the y-stress along the structure

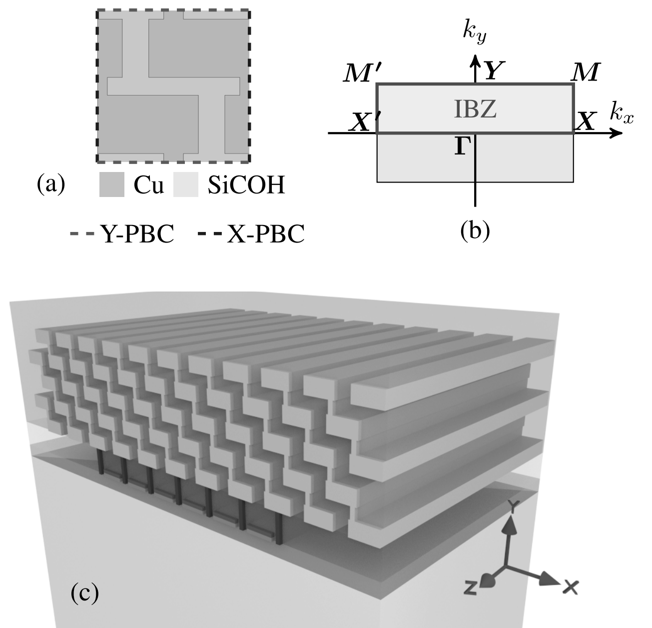

Fig. 5. (a) A Z-shaped Unit cell for a PnC implemented in IBM 32 nm SOI technology BEOL, with only inversion symmetry. Blue and green dashed lines indicate the periodic boundary conditions applied in FEM simulation. (b) First Brillouin Zone and IBZ of the reciprocal lattice for the unit cell of (a). (c) 3D view of the full PnC on top of an RBT.

is shown in Fig. 4(b), demonstrating standing waves formed between the source and the PnC. The y-stress transmitted through the PnC is lower than the standing wave amplitude before the PnC by 57 dB and 89 dB at 2.8 GHz and 4.45 GHz, respectively. The strong evanescent decay of the stress signal inside the BEOL CMOS layers demonstrates the efficiency of this PnC implementation, despite the limited number of metal layers available in the CMOS technology under consideration.

The unit cell of an alternative PnC implemented in IBM 32 nm SOI is shown in Fig. 5(a). This PnC makes use of the copper vias together with the metalization to create a Z-like shape. The copper stripes have a width of 125 nm and a spacing of 67 nm, both in x-direction. The only symmetry operation for this structure is inversion symmetry, and hence the IBZ consists of two coinciding rectangles in the first Brillouin Zone as shown in Fig. 5.b. This is the case since time reversal symmetry sets $\omega(\vec{k}) = \omega(-\vec{k})$ and thus, two coinciding rectangles are enough to determine the IBZ in the most general case, even with the absence of any structural symmetry for the unit cell. The dispersion relation of this PnC is shown in Fig. 6, which shows two major bandgaps of width 1.13 GHz (2.23 GHz-3.36 GHz) and 1.07 GHz (7.13 GHz-8.2 GHz).

Yet another CMOS PnC implementation is studied in XFab 0.18 μm BEOL layers. The unit cell is shown in Fig. 7, whereas its dispersion relation is shown in Fig. 8. This PnC is based on tungsten vias surrounded by SiO_2 inter-metal dielectric. As can be seen from Table I, these materials have large acoustic impedance contrast, making them ideal for constructing PnCs with large bandgaps. With 850 nm tungsten vias separation, a 13% fractional bandgap (250 MHz from 1.80 GHz to 2.05 GHz) is obtained . Another interesting feature of the PnC in XFab 0.18 μm technology is the relatively small impedance mismatch between aluminum and SiO_2.

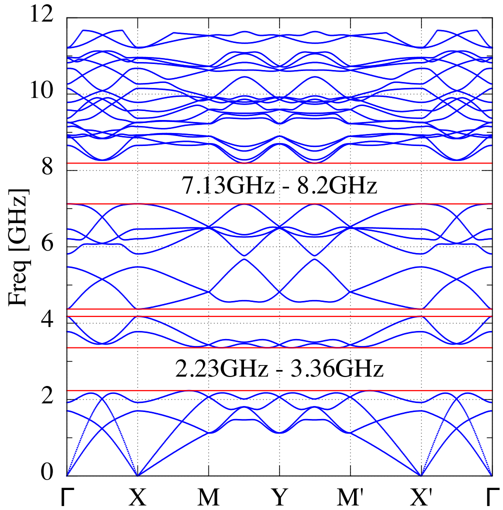

Fig. 6. Dispersion relation for the PnC of Fig. 5 implemented in IBM 32 nm SOI, showing bandgaps of 1.13 GHz (2.23 GHz - 3.36 GHz) and 1.07 GHz (7.13 GHz - 8.2 GHz).

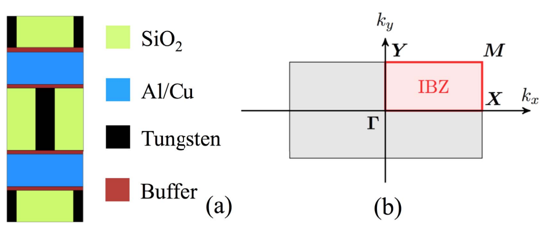

Fig. 7. (a) Unit cell for a PnC implemented in XFab 0.18 μm technology BEOL. (b) First Brillouin Zone and IBZ of the reciprocal lattice for the unit cell of (a).

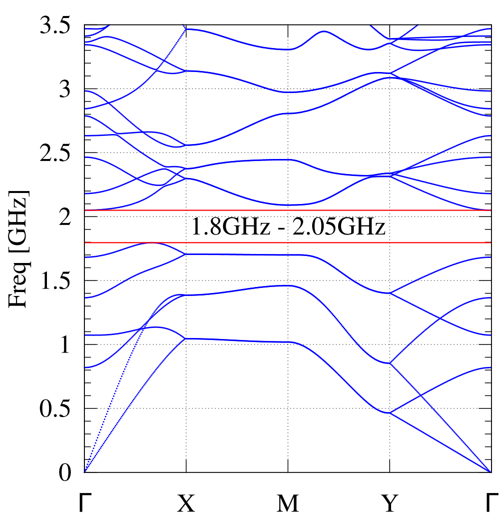

Fig. 8. Dispersion relation for the PnC of Fig. 7 implemented in XFab 0.18 μm bulk CMOS technology, showing a bandgap of 250 MHz (1.80 GHz - 2.05 GHz).

This gives an extra degree of freedom for the aluminum routing traces without compromising the mechanical performance of the PnC. Furthermore, the lower wave velocity in SiO_2 compared to aluminum, creates the possibility for index guiding between the aluminum layers, which further improves the performance of such PnCs.

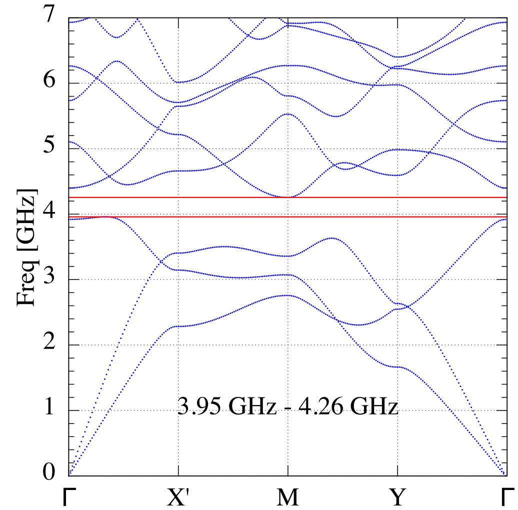

Fig. 9. Dispersion relation for a typical PnC in IBM 0.13 μm technology, showing a bandgap of 310 MHz (3.95 GHz - 4.26 GHz).

TABLE II
PERFORMANCE SUMMARY OF DIFFERENT CMOS PnC CONSIDERED IN THIS STUDY

Technology	IBM			XFab
	32 nm SOI	32 nm SOI	0.13 μm	0.18 μm
Unit Cell	Fig. 2(a)	Fig. 5(a)	Fig. 2(a)	Fig. 7(a)
$\omega - \vec{k}$	Fig. 3	Fig. 6	Fig. 9	Fig. 9
Dielectric	low-κ SiCOH		SiO_2	SiO_2
Scatterers	Cu	Cu	Cu	W
Z_{11} ratio	19	19	3	7.5
Z_{44} ratio	15.9	15.9	2.3	6.6
Bandgap Width [GHz]	3.8	1.13 1.07	0.3	0.72 0.46
Bandgap Center [GHz]	4.45	2.8 7.67	4.1	1.79 2.92

A PnC in IBM 0.13 μm technology with similar unit cell to that of Fig. 2(a) is also considered. In this particular technology, the routing layers are formed from copper metallization surrounded by SiO_2 isolation. The dispersion relation for a typical PnC in this technology is shown in Fig. 9. This PnC shows a bandgap of 310MHz (7% fractional bandgap) for 300 nm-wide metal lines with 200 nm separation. Such bandgap was found to be among the highest attainable in this technology. Since the contrast between the acoustic impedance of copper and oxide is not as strong for the case of Cu/SiCOH or W/SiO_2, and since the DRC restrictions that forces the metal segments to be far apart, the resulting bandgap is much smaller than that obtainable in the other technologies. Moreover, this technology has layer thickness variations that significantly exceed its fractional bandgap. The performance of this PnC will be sensitive to process variations, significantly limiting its usability for practical implementations. Table II summarizes the material composition and performance of all the PnCs considered in this work.

C. CMOS Process Variations and PnCs

Random process variations inherent to CMOS processes represent a non-trivial challenge for PnC implementation

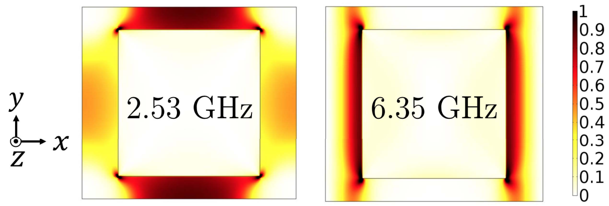

Fig. 10. Normalized stored strain energy distribution for the PnC unit cell of Fig. 2(a), plotted for modes at the edges of the PnC bandgap with $k_x = 0$ and $k_y = 0$.

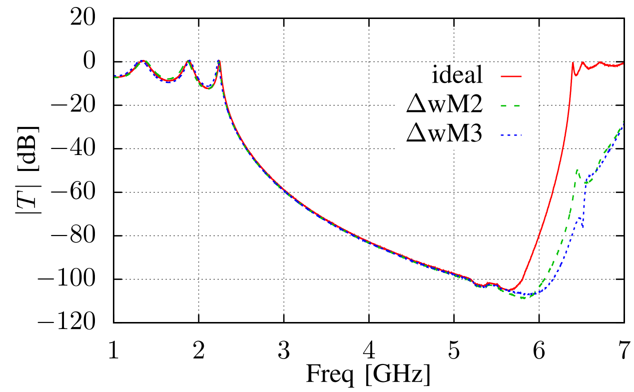

Fig. 11. Transmission coefficient through PnC of Fig. 2(a) with variation in the metal lines width. ΔwM2 and ΔwM3 indicates +20 nm individual change in the width (in x-direction) of metal 2 and 3 respectively.

therein. Variations in BEOL layer thicknesses, metal widths and lithographic misalignment are notable examples. Guided by the intuition from (19), it is clear that uniform structure scaling will result in proportional scaling for the PnC dispersion relation. However, the aforementioned CMOS process variations are random in nature, which creates a *mismatch* between the different PnC layers.

To study the effect of such process variations, we turn our attention to a powerful result from perturbation theory. Small perturbations to the structure geometry induce a frequency shift $\Delta\omega$ that is given by [27]:

$$\frac{\Delta\omega}{\omega^0} = \frac{1}{2}\left(\frac{\Delta U}{U^0} - \frac{\Delta K}{K^0}\right) \tag{22}$$

where U and K are the stored potential and kinetic energy, respectively. The superscript 0 denotes the unperturbed modes. $\Delta U = U - U^0$ and $\Delta K = K - U^0$ represent the change in the stored energies due to perturbation. The thicknesses variation and mismatch in dimensions under consideration involves shifting of the material boundaries. Equation (22) indicates that modes with significant energy stored near to the perturbation location (the shifted boundary in this case) are more likely to experience larger frequency shifts. Although such variations can not be considered *small* perturbations [33], the former intuition in terms of stored energy remains valid. Accurate FEM simulation are necessary to obtain numerical results on the effect of each variation type.

The detailed effect of process variations strongly depend on the PnC geometry and material composition. The PnC of Fig. 2(a) will be considered as a case study to assess the effect of CMOS process variations on its performance. Fig. 10 shows the normalized strain energy distribution within the unit cell of the aforementioned PnC, for the modes at the bandgap edges, with $k_x = 0$ and $k_y = 0$. Layer thickness and metal width variation affect each of these modes differently, depending on the distribution of stored energy.

The PnC unit cell model is not helpful in studying perturbations to individual layers. For this reason, the 2D FEM model of Fig. 4(a) is used in a frequency domain simulation to find the transmission coefficient $\boldsymbol{T}$ of the PnC, defined as:

$$|\boldsymbol{T}| = \left|\frac{T_t}{T_i}\right| \tag{23}$$

where T_t and T_i are the transmitted and incident stresses respectively. By exploiting the similarity between the elastic and electro-magnetic wave, this problem can be approached as a transmission line problem [26]. The transmitted stress T_t is directly found from the amplitude of the travelling wave after the PnC. The incident stress T_i is found from the standing wave formed before the PnC, by first finding the standing wave ratio (SWR):

$$\mathrm{SWR} = \left|\frac{T_{\max}}{T_{\min}}\right| \tag{24}$$

where $T_{\max}$ and $T_{\min}$ are the maximum and minimum stresses of the standing wave respectively. The reflection coefficient $\boldsymbol{\Gamma}$ and hence the incident stress are then found as:

$$|\boldsymbol{\Gamma}| = \left|\frac{T_i}{T_r}\right| = \frac{\mathrm{SWR}-1}{\mathrm{SWR}+1} \tag{25}$$

$$T_i = \frac{T_{\max}}{1+|\boldsymbol{\Gamma}|} \tag{26}$$

where T_r is the reflected stress.

First, the width of individual metal layers is changed, emulating one of the possible mismatches in the PnC. From the energy distribution of Fig. 10, it is expected that the mode at 6.35 GHz will experience larger frequency shifts, since the stored energy is localized around the metal line side walls. Fig. 11 compares the transmission coefficient of an ideal PnC to one that is subject to such mismatch. The upper bandgap edge (at 6.35 GHz) is more affected by such variation in comparison to the lower edge. No spurious transmission is observed for such variation.

Next, the thickness of the metal and via layers are perturbed by 20% of their nominal thickness. The energy distribution of Fig. 10 predicts that the lower bandgap edge mode at 2.53 GHz will undergo larger frequency shifts than the upper bandgap edge. This is mainly due to the large stored energy concentration around the metal lines top and bottom surfaces. Fig. 12 and Fig. 13 present the transmission coefficients for PnCs with such perturbation. Both figures clearly highlight the larger shift in the lower bandgap edges. Maximum shifts of 74 MHz and 142 MHz are observed in the lower bandgap edges for the metal layer and via thickness perturbation, respectively. Perturbations to both individual layers and multiple layers are tested. It is important to notice that for a PnC restricted to 5 layers, the PnC performance is symmetric; perturbing

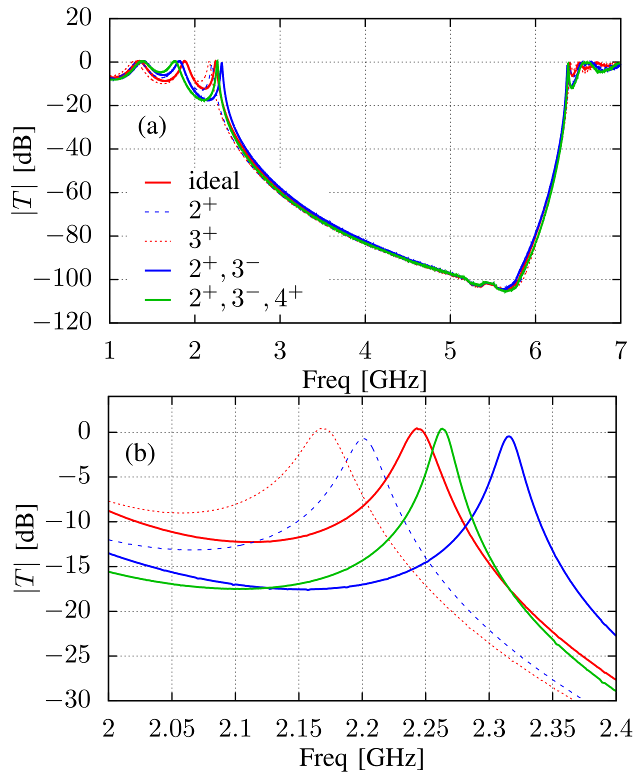

Fig. 12. (a) Effect of different metal layer thickness variation on the transmission coefficient through the PnC of Fig. 2. $n^{\pm}$ indicate a $\pm 20\%$ change in the thickness of the n^{th} layer (b) Zoomed in version of (a) around the lower PnC band edge.

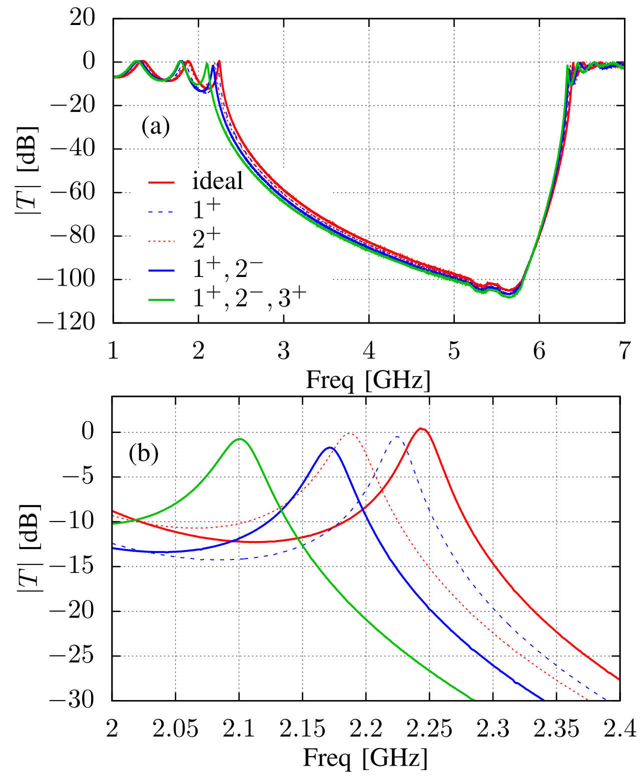

Fig. 13. (a) Effect of different via layer thickness variation on the transmission coefficient through the PnC of Fig. 2. $n^{\pm}$ indicate a $\pm 20\%$ change in the thickness of the n^{th} via layer (b) Zoomed in version of (a) around the lower PnC band edge.

M4 layer is equivalent to perturbing M2 layer. Again, no spurious transmission is observed for this type of variation.

Lithographic misalignment between the different metal layers is considered next. A 20 nm misalignment between the metal layers is assumed. Fig. 14 shows the resulting transmission both for individual layers misalignment along with 2 and 3 layers simultaneous misalignment. First, the upper edge of the bandgap is affected by such misalignment, as expected from the stored energy distribution. More importantly, a spurious transmission mode is created around 2.55 GHz. Basically, the misalignment creates a line defect resonance cavity in the PnC, which introduces a defect mode in the PnC bandgap. Evanescent modes in the PnC couple energy to this cavity, creating the transmission spur [16]. The sharp dip in the transmission indicates a spurious change in the reflectivity and hence the acoustical impedance presented by the PnC to the RBT structure. Such spurs have the potential of creating spurious modes in the RBT frequency response, if the corresponding stress-strain field distribution can be driven and sensed by the RBT transducers.

In conclusion, for the PnC of Fig. 2, reasonable process variation and mismatch mostly affect the PnC characteristics near its bandgap edges. In case of PnCs with wide bandgaps, the PnC characteristics are negligibly affected near the center of the bandgap. Achieving wide bandgaps through materials and dimensions selection is thus necessary for PnC implementation in CMOS for several reasons: (i) Decay rate of evanescent waves in the PnC depends on the frequency separation from bandgap edges, hence wider bandgap ensures faster decay. (ii) Faster wave decay enables high reflectivity with a small number of layers (a common limitation of CMOS processes), (iii) The wide bandgap provides larger tolerance for random process variations and different mismatches. This explains why the PnC implemented in IBM 0.13 μm (Fig. 9), with a fractional bandgap of 7% is highly unreliable for practical implementations as discussed in section II-B.

III. RBT Structure

The authors have previously demonstrated a CMOS-RBT in [7] that relied solely on acoustic Bragg reflectors (ABRs) for acoustic confinement [34]. While this was the first demonstration of unreleased CMOS-MEMS resonators, this resulted in a significantly low quality factor $Q < 30$ due to small solid angle subtended by the ABRs, and hence increased radiation losses both through the substrate and the BEOL layers. Moreover, the drive and sense transducers each spanned half the cavity depth, resulting in significant scattering which also contributed to the radiation losses and reduced Q.

A. PnC-Based Acoustic Waveguide

Before considering the full PnC-RBT, a much simpler structure with only the BEOL PnC and unpatterned FEOL layers (excluding contacts) on top of the bulk wafer is studied. Such structure is periodic in the x-direction with the same period as the PnC. Only a vertical section with x-periodic boundary

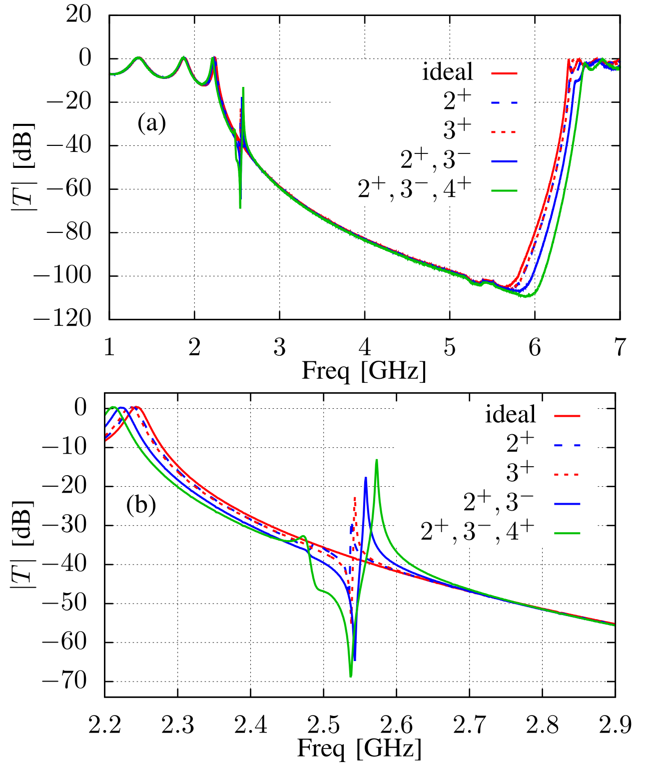

Fig. 14. (a) Effect of different metal layers lithographic misalignment on the transmission coefficient through the PnC of Fig. 2. $n^{\pm}$ indicate a ± 20 nm misalignment in the x-direction for the n^{th} metal layer (b) Zoomed in version of (a) around the spurious transmission.

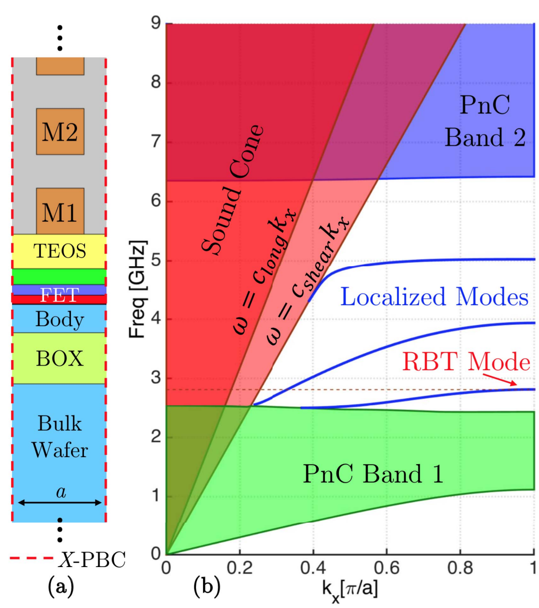

Fig. 15. (a) Vertical section of the PnC of Fig. 2(a) showing FEOL layers and the wafer bulk with x-periodic boundary conditions (X-PBC). (b) Dispersion relation from FEM simulation showing PnC bands, sound cone and localized modes.

conditions (x-PBC) is considered as shown in Fig. 15(a). The dispersion relation of such a structure is found by means of a 2D plane strain FEM simulation. Owing to its periodicity in x-direction, only the k_x component of the $\vec{k}$-vector is conserved throughout the entire structure. Thus, k_x is used

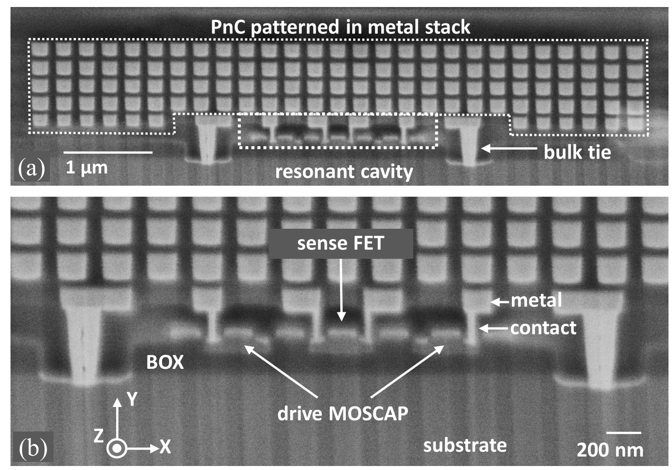

Fig. 16. (a) SEM micrograph of an unreleased RBT implemented in IBM 32 nm SOI technology, showing a phononic crystal patterned in the BEOL metal stack. (b) A detailed micrograph of the resonant cavity showing the driving MOS-Caps along with the sensing FET.

to classify the modes in the dispersion relation as shown in Fig. 15(b). Different types of modes can be observed in the dispersion relation [28]:

- *Bulk Propagating Modes:* These are plane waves propagating in the bulk wafer. Their dispersion relation is simply given by:

$$\omega = c|\vec{k}| = c\sqrt{k_x^2 + k_y^2} \tag{27}$$

  where c is the wave velocity (being longitudinal or shear waves). Thus, for a given k_x, the allowed modes in the bulk form a continuum $\omega > c\,k_x$, referred to as the *sound-cone* and bounded by the *sound-line* $\omega = c\,k_x$.
- *PnC Propagating Modes:* These modes form continuous bands corresponding the PnC bands (bands 1 and 2).
- *Bulk Evanescent Modes:* These are modes below the sound-line, with $\omega < c\,k_x$ and imaginary k_y. They decay exponentially in the bulk in the y-direction. This phenomenon corresponds to the total internal reflection in optics.
- *PnC Evanescent Modes:* These modes are located in the PnC bandgap, they decay exponentially in the PnC. These modes are not shown in the PnCs' dispersion relations since they do not exist in infinite, perfectly-periodic structures.
- *Localized Modes:* These modes are both below the sound-cone and in the PnC bandgap. Such modes show evanescent exponential decay in both the PnC and bulk.

The localized modes are spatially confined in the FEOL layers between the PnC and the bulk silicon wafer. Without further constraints in the lateral dimensions, wave propagation is allowed between the PnC and bulk wafer in the $x - z$ plane, forming a horizontal waveguide. The full RBT geometry, with the actual gates, contacts and finite width, creates the constraints necessary for horizontal confinement.

B. PnC-Based RBT Design

Fig. 16 shows a cross-section SEM micrograph of the RBTs proposed in this work and implemented in IBM 32 nm

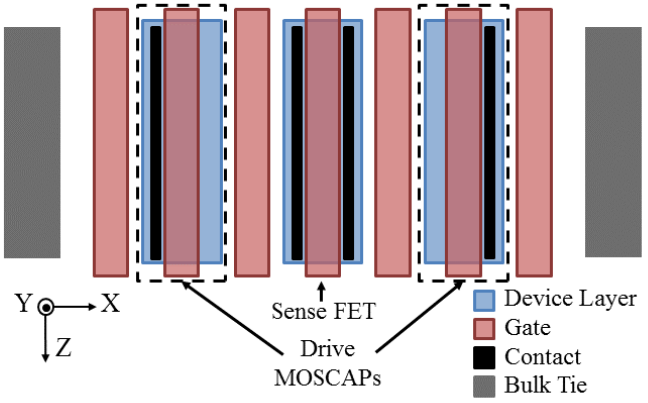

Fig. 17. Top view of PnC resonator layout showing drive and sense transistors, gates, modified contacts, first metal level and bulk ties. Metal layers are excluded for clarity of underlying structure.

SOI technology. This RBT relies on a PnC constructed in the CMOS BEOL layers to achieve vertical acoustic confinement. The main RBT mode is a localized mode with evanescent decay in both the PnC and the bulk as discussed in section III-A. A distribution of k_x values (near $k_x = \pi/a$) is enforced by the driving mechanism spatial configuration, hence exciting specific modes from the dispersion relation of Fig. 15(b).

The presented RBT uses the foundry-provided analog nFET both for sensing and electrostatic driving. This allows the RBT to harness the ultra-thin, high quality gate dielectric for efficient driving by internal dielectric transduction, as well as the highly reliable, high-f_T nFETs for active transistor sensing [7], [9]. The non-uniform cavity cross-section was addressed by setting two nFETs for driving as MOS capacitors (MOSCAPs) that span the entire depth of the resonance cavity in the y-direction, as shown in Fig. 17. A single sensing nFET was included at the center of the cavity between the two driving MOSCAPs. The advantage of FET sensing in CMOS RBTs over other transduction mechanisms is discussed elsewhere [7]. A floating-body nFET was chosen for sensing over a body-contacted one to reduce the cavity perturbations in the y-direction. Moreover, the drive and sense gate routing was limited to the first metal layer, in order to preserve the PnC translational symmetry in the higher metal layers. This represents one of the challenges of this RBT design, since the electrical routing affects the mechanical properties of the structures. The enhanced cavity uniformity along its depth is very important in reducing the scattering and radiation losses as will be further demonstrated in section III-C.

The structural integrity of the FETs must be maintained to avoid compromising their performance. For this reason, the foundry-included dummy gates for the sensing FET were left unmodified. They also help preserve the uniformity of the stress liner, which is crucial for setting the FET channel mobility. Adjacent transistors in the resonant cavity were positioned in a way to ensure an exact overlap between their dummy gates. The current implementation uses nFETs with 160 nm gate length, 2 μm width and gate-to-gate pitch of 290 nm.

To achieve optimal acoustic confinement, modification of some foundry-provided layout parameters was necessary. Drain-side contacts from the MOSCAP were removed to minimize acoustic scattering points within the resonant cavity itself. Moreover, long, rectangular, wall-like vias spanning the entire width of the FET were used as shown in Fig. 17. This was selected over traditional CMOS square contacts for better uniformity along the y-direction. Finally, large bulk ties (vias to substrate) were included to assist with horizontal mode confinement, as shown in Fig. 16.

It is important to emphasize the fact that the SOI buried oxide layer (BOX) is not contributing to the mechanical confinement and the same concept is seamlessly amenable to bulk CMOS technologies. In fact, the BOX layer (with lower acoustic velocity) located between the bulk and the silicon active device area (with higher acoustic velocity) acts as slab waveguide. Such waveguide must be carefully considered as coupling from the RBT cavity may lead to significant energy losses and quality factor degradation. However, the k_x component enforced by the driving mechanism and the PnC periodicity, together with the narrow thickness of the BOX layer, hinder such coupling for the frequencies under consideration. The localized modes of interest (near $k_x = \pi/a$) fall entirely under the sound-line of SiO_2, as $\omega < c_{SiO_2} k_x$. Thus, the RBT mode exhibits exponential evanescent decay in the BOX layer as well. The major advantage of the BOX layer is to provide better electrical isolation between the drive and sense transducers, inherently reducing the direct feed-through. In bulk CMOS technologies, RF transistor isolation techniques such as deep nwells and guard rings may be used, though this may increase the overall resonator footprint.

C. Cavity Uniformity and Perturbations

The RBT cavity is assumed to have a depth W in the z-direction. 2D plane strain analysis is a good approximation when the cavity depth W is much larger than the characteristic dimensions in the transverse (x, y) plane, and consequently the wavelength λ. Basically, this condition allows us to consider the cavity as a long wave guide in the z-direction with *local* continuous translation symmetry over sufficiently long distances, and hence, studying its cross-section becomes a reasonable approximation. To understand the effect of the cavity's finite depth and other perturbations along the z-axis, it proves useful to consider coupled mode theory [35]–[38]. The modes obtained from the 2D cross-section analysis of the cavity are considered *local* modes, in the sense that they may slowly evolve along the z-direction [35]. Considering a set of orthogonal local wave solutions with stresses $T_n(x, y)$ and displacements $u_n(x, y)$ to be column vectors $|n\rangle_z = [T_n(x, y), u_n(x, y)]^T$, the coupled mode theory suggests that the solution along z-direction can be approximated as:

$$|\psi(z)\rangle = \sum_n c_n(z)\, |n\rangle_z\, e^{i\int dz\beta_n(z)} \tag{28}$$

for some coefficients $c_n(z)$ and z-component β_n of the wave vector $\vec{k}$. By following the analysis in [35], a system of

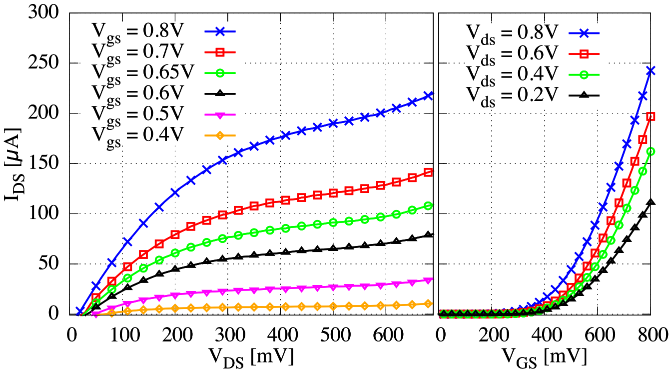

Fig. 18. (left) $I_{DS} - V_{DS}$ characteristics and (right) $I_{DS} - V_{GS}$ of the resonator's sensing FET showing expected transistor response. In operation, the the sensing FET was biased at $V_{DS} = 0.6\,\text{V}$ and $V_{GS} = 0.65\,\text{V}$.

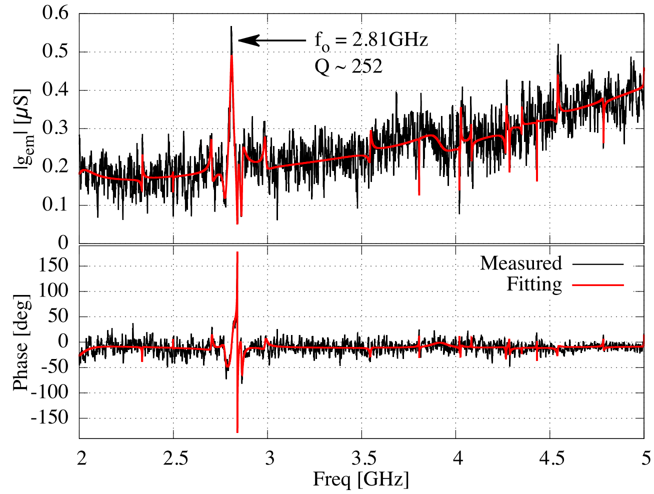

Fig. 19. Measured electromechanical transconductance g_{em} of the IBM 32nm SOI RBT of Fig. 16

ordinary differential equations is obtained for the coefficients $c_n(z)$ which has the general form of:

$$2k_m \frac{d}{dz} c_m + c_m \nabla_{tr} \cdot \vec{k} = \sum_{n \neq m} e^{i\Delta\beta_{nm}} A_{mn} c_n \tag{29}$$

where $k_m = |\vec{k}_m|$, ∇_{tr} is the differential nabla operator in transverse x, y directions, $\Delta\beta_{nm} = \beta_n - \beta_m$ and A_{mn} are the mode coupling matrix coefficients, related to the specific mode shape as well as the spatial rate of change of the stiffness and density of the cavity materials [35], [37].

Equation (29) suggests that cavity perturbations will result in *scattering*: the energy of each mode is no longer conserved, and energy can be exchanged between modes with different $\vec{k}$ vectors (yet still at the same frequency). Such scattering will be directly manifested as a reduced quality factor Q and the generation of more spurious modes in the resonator frequency response. The cavity's abrupt termination also results in increased radiation in the bulk material, reducing the Q of the resonator even further. This emphasizes the importance of the uniformity of the cavity along its depth W and the need for slow and smooth transitions whenever structurally possible [37] for creating high Q resonators with spurious-free spectrum. Although coupled-mode theory in this regard may not be useful for direct numerical calculations (since terminating the resonance cavity cannot be considered a small perturbation), the implications of increased scattering with perturbations remains true. Section IV presents measurement results that highlight the effects of perturbations in the resonance cavity.

IV. Results

The unreleased RBTs presented in this work were fabricated as part of the standard IBM 32 SOI process without additional post-processing or special packaging of any kind. The RBT of Fig. 16 is considered to be the typical design in this work and occupies an area of $5\,\mu m \times 7\,\mu m$. The measured DC characteristics of the sensing FET are shown in Fig. 18, which closely match the projected performance based on the provided IBM design kit, despite the modifications mentioned in section III. For normal RF operation, the driving MOSCAP gates are biased in inversion with $V_A = 1\,V$ while the sensing transistor is biased in saturation with a grounded source, while drain and gate voltages are set for $V_{DS} = 0.6\,V$ and $V_{GS} = 0.65\,V$, respectively. The drain current in the sensing FET in this case is $I_{DS} = 95\,\mu A$, well within the electromigration limits of the RBT routing metals. Spice simulations based on the IBM provided design kit model show that operating the sensing transistor in saturation maximizes the drain current sensitivity to the relative change in the channel mobility, and hence maximizes the electromechanical transconductance efficiency g_{em}/I_{DS} of the device. The saturation regime also has the benefit of maximizing the output resistance of the FET which greatly simplifies the subsequent design of current readout circuits.

A Cascade PMC200 RF probe system was used to test the presented RBTs. TRL calibration up to the GSG probe tips was carried out at room temperature with $-10\,$dBm input power and 2 kHz IF bandwidth with 50 averaging traces using an Agilent PNA N5225A. A continuous N_2 purge was used during testing to reduce the risk of electrostatic discharge (ESD) events and help protect the devices during extended testing. The overall input-to-output electromechanical transconductance g_{em} is obtained from the de-embedded Y-parameters as per standard MOSFET measurements:

$$g_{em} = i_{out}/v_{in} = Y_{21} - Y_{12} \tag{30}$$

Electrical parasitics of the RBT were de-embedded using its own response at $V_A = 0\,V$ on the driving MOSCAP, corresponding to the resonator "Off" state to suppress the mechanical modes. The measured g_{em} frequency response of a 2.8 GHz resonator is presented in Fig. 19. An 11-point running average filter is applied to smooth the measured data. This smoothing is a highly conservative operation that may slightly reduce the quality factor of the resonator peak. After smoothing, a rational transfer function fitting [39] with 24 poles was used to extract a Q of 252 at the 2.8 GHz resonance peak, leading to an $f \times Q = 7 \times 10^{11}$. By virtue of the superior confinement achieved by the PnC, the presented RBT design shows an $8\times$ improvement in Q ($2.5\times$ in $f \times Q$)

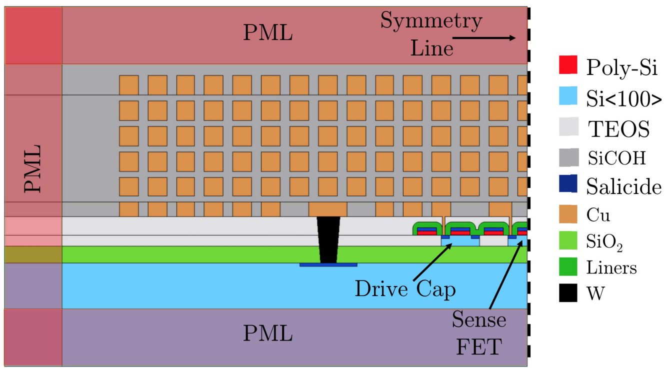

Fig. 20. FEM model for the RBT structure, showing PMLs (scaled for better presentation) and symmetry boundary conditions.

over the previous generation CMOS-integrated RBTs in [7] with only a 2× increase in the overall footprint. At such frequencies, the dominant phonon relaxation mechanism is the Landau-Rumer regime, where the $f \times Q$ product increases linearly with frequency [40]. Since both resonators' $f \times Q$ product is significantly lower than the expected theoretical limits of most materials, the quality factor is not limited by phonon relaxation in any of them. Instead, radiation loss from the cavity dominates the quality factor of both devices. For this reason, the PnC RBT shows a major improvement in the quality factor Q. The PnC RBT also shows a wider spurious-free spectral range extending up to 4.5 GHz.

A frequency domain, 2D plane-strain-approximation FEM simulation is carried-out for a cross section of the RBT structure. COMSOL Multiphysics solid-mechanics module is used [31]. The FEM model is shown in Fig. 20, where only half the RBT structure is considered with symmetry boundary conditions. The model is calibrated with the fabricated dimensions as found from the SEM micrograph (including individual PnC layer thicknesses). PMLs surround the RBT to prevent reflections to the resonance cavity, hence approximating the radiation losses. Stress load is applied to the driving MOSCAPs, corresponding to the actual electrostatic stress generated by the transducer. The resulting average stresses in the sensing transistor channel area are shown in Fig. 21. The measurement results are found to be in good agreement with the simulation predictions for the resonance frequencies. The spurious mode at 4.6 GHz corresponds to the high-frequency mode of the simulation but is not distinguishable above the feedthrough floor and has intrinsically lower Q. The measured Q was expected to be lower than the simulated Q value of 962 for the following reasons:

(a) The inter-metal dielectric is a porous SiCOH (pSiCOH) ultralow-κ dielectric [41] and is expected to be a significant source of viscoelastic damping [42]. However, relevant material parameters could not be disclosed by the foundry, or were unknown and hence viscoelastic damping was not included in the simulation, which only considers lateral radiation losses from the cavity (in the $x-y$ plane).

(b) The simulation is a 2D plane strain approximation and does not account for the scattering due to the finite cavity depth as well as its abrupt termination as discussed in section III-C.

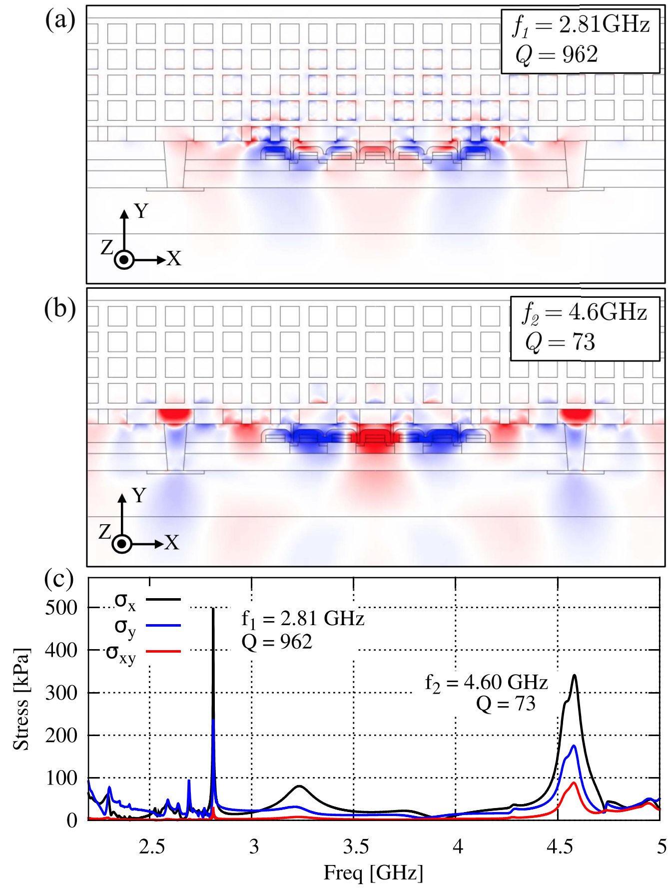

Fig. 21. (a) X-stress at 2.81 GHz in 2D PnC-RBT structure showing Q of 962. (b) X-stress in resonant structure at 4.6 GHz with Q of 73. (c) Frequency response from 2D FEM COMSOL simulation of the RBT, showing the average stresses in the channel area with resonances at 2.81 GHz (Q of 903) and 4.5 GHz.

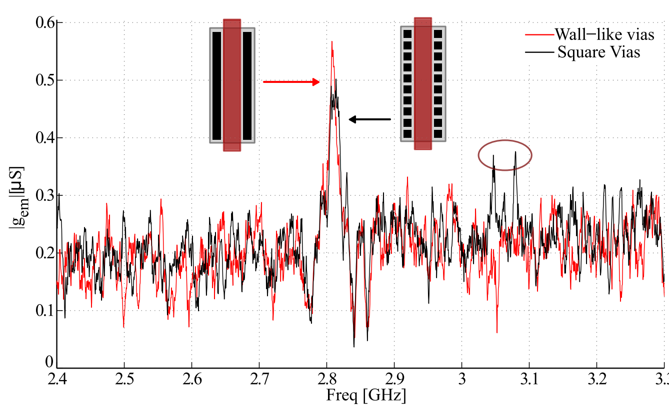

Fig. 22. Measured electromechanical transconductance g_{em} for identical RBTs with rectangular (*wall-like*) vias and the regular CMOS square vias. The device with square vias has clearly reduced quality factor Q and extra spurious modes.

To emphasize the effect of structural perturbations on resonator performance, the electromechanical transconductance g_{em} of the previously discussed RBT is compared to an identical one designed using standard square vias. The RBT of Fig. 16 includes long rectangular (wall-like) vias that span the entire depth of the cavity for contacting the driving MOSCAPs and the sensing FET. This structure provides a substantial uniformity in the depth direction (z-direction), and hence minimizing the scattering as discussed in section III-C. Fig. 22 compares the performance of the aforementioned RBT to an identical one, except for using standard CMOS square vias. Both RBTs were fabricated on the same die and are expected to have closely matched layer thicknesses, as justified by the exact overlap of their resonance frequency. The square-via RBT clearly suffers from a reduced peak height, a reduced quality factor Q of 160, as well as the introduction of multiple spurious modes. This clearly verifies the prediction of the coupled-mode theory from section III-C and underlines the importance of uniformity and smooth transitions in cavity design.

V. Conclusion

Implementation and design of phononic crystals in the BEOL layers of commercial CMOS technologies has been explored. The benefits of using such PnCs for acoustic confinement of unreleased CMOS RBTs has been highlighted. The lithographically defined PnC dimensions allow for bandgap engineering, providing a flexibility in resonator design, and allows for multiple frequencies on chip. Theoretical analysis of phononic crystals has been presented, together with the focus on the specific details concerning CMOS implementation. PnC designs in different CMOS technologies have also been presented and compared. Fabrication variations and cavity non-uniformity degrades the resonator quality factor and allows for spurious modes, where the latter have been experimentally verified in this work. For reliable CMOS RBT design, PnCs are required to have large bandgaps around their resonance frequency. This can be achieved in CMOS technologies that provide BEOL materials with large acoustic impedance contrast, and the ability to pattern smaller dimensions for GHz-frequencies. With the help of the 85% fractional bandgap PnC demonstrated in this work, second-generation RBTs were able to achieve a quality factor Q of 252, $8\times$ higher than the previous generation RBTs, in IBM 32nm SOI technology.

Acknowledgment

The authors would like to thank Prof. Steven Johnson from MIT for the invaluable discussion and feedback.

References

[1] G. K. Fedder, R. T. Howe, T.-J. K. Liu, and E. P. Quevy, "Technologies for cofabricating MEMS and electronics," *Proc. IEEE*, vol. 96, no. 2, pp. 306–322, Feb. 2008.

[2] H. Xie, L. Erdmann, X. Zhu, K. J. Gabriel, and G. K. Fedder, "Post-CMOS processing for high-aspect-ratio integrated silicon microstructures," *J. Microelectromech. Syst.*, vol. 11, no. 2, pp. 93–101, Apr. 2002.

[3] C.-S. Li, L.-J. Hou, and S.-S. Li, "Advanced CMOS–MEMS resonator platform," *IEEE Electron Device Lett.*, vol. 33, no. 2, pp. 272–274, Feb. 2012.

[4] C. B. O'Neal, A. P. Malshe, S. B. Singh, W. D. Brown, and W. P. Eaton, "Challenges in the packaging of MEMS," in *Proc. Int. Symp. Adv. Packag. Mater., Process., Properties, Interf.*, Mar. 1999, pp. 41–47.

[5] K. Persson and K. Boustedt, "Fundamental requirements on MEMS packaging and reliability," in *Proc. 8th Int. Symp. Adv. Packag. Mater.*, 2002, pp. 1–7.

[6] A. Morris and S. Cunningham, "Challenges and solutions for cost-effective RF-MEMS packaging," in *Proc. 32nd IEEE/CPMT Int. Electron. Manuf. Technol. Symp. (IEMT)*, Oct. 2007, pp. 278–285.

[7] R. Marathe, B. Bahr, W. Wang, Z. Mahmood, L. Daniel, and D. Weinstein, "Resonant body transistors in IBM's 32 nm SOI CMOS technology," *J. Microelectromech. Syst.*, vol. 23, no. 3, pp. 636–650, Jun. 2014.

[8] M. S. Kushwaha, P. Halevi, L. Dobrzynski, and B. Djafari-Rouhani, "Acoustic band structure of periodic elastic composites," *Phys. Rev. Lett.*, vol. 71, pp. 2022–2025, Sep. 1993.

[9] M. S. Kushwaha, P. Halevi, G. Martinez, L. Dobrzynski, and B. Djafari-Rouhani, "Theory of acoustic band structure of periodic elastic composites," *Phys. Rev. B*, vol. 49, pp. 2313–2322, Jan. 1994.

[10] Y.-F. Wang, Y.-S. Wang, and X.-X. Su, "Large bandgaps of two-dimensional phononic crystals with cross-like holes," *J. Appl. Phys.*, vol. 110, no. 11, p. 113520, 2011.

[11] B. Bahr, R. Marathe, and D. Weinstein, "Phononic crystals for acoustic confinement in CMOS–MEMS resonators," in *Proc. IEEE Int. Freq. Control Symp. (FCS)*, May 2014, pp. 1–4.

[12] M. Ziaei-Moayyed, M. F. Su, C. M. Reinke, I. El-Kady, and R. H. Olsson, III, "Silicon carbide phononic crystals for high $f.Q$ micromechanical resonators," in *Proc. IEEE Ultrason. Symp. (IUS)*, Oct. 2010, pp. 162–166.

[13] N.-K. Kuo and G. Piazza, "1 GHZ phononic band gap structure in air/aluminum nitride for symmetric lamb waves," in *Proc. IEEE 24th Int. Conf. Micro Electro Mech. Syst. (MEMS)*, Jan. 2011, pp. 740–743.

[14] S. Wang, L. Popa, and D. Weinstein, "GaN MEMS resonator using a folded phononic crystal structure," in *Proc. Solid-State Sens., Actuators, Microsyst. Workshop (Hilton Head)*, 2014, pp. 72–75.

[15] C. Y. Koh, "Generalized phononic networks of length scales, symmetry breaking and (non) locality," Ph.D. dissertation, Dept. Mater. Sci. Eng., Mass. Inst. Technol., Cambridge, MA, USA, 2011.

[16] A. Khelif, A. Choujaa, B. Djafari-Rouhani, M. Wilm, S. Ballandras, and V. Laude, "Trapping and guiding of acoustic waves by defect modes in a full-band-gap ultrasonic crystal," *Phys. Rev. B*, vol. 68, p. 214301, Dec. 2003. [Online]. Available: http://link.aps.org/doi/10.1103/PhysRevB.68.214301

[17] R. Ruby, P. Bradley, J. Larson, III, Y. Oshmyansky, and D. Figueredo, "Ultra-miniature high-Q filters and duplexers using FBAR technology," in *IEEE Int. Solid-State Circuits Conf., Dig. Tech. Papers (ISSCC)*, Feb. 2001, pp. 120–121.

[18] R. Aigner, J. Ella, H.-J. Timme, L. Elbrecht, W. Nessler, and S. Marksteiner, "Advancement of MEMS into RF-filter applications," in *Proc. IEEE Electron Devices Meeting (IEDM)*, Dec. 2002, pp. 897–900.

[19] D. Weinstein and S. A. Bhave, "The resonant body transistor," *Nano Lett.*, vol. 10, no. 4, pp. 1234–1237, 2010.

[20] A. M. Ionescu, "Resonant body transistors," in *Proc. Device Res. Conf. (DRC)*, Jun. 2010, pp. 181–182.

[21] S. T. Bartsch, C. Dupre, E. Ollier, and A. M. Ionescu, "Resonant-body silicon nanowire field effect transistor without junctions," in *Proc. IEEE Int. Electron Devices Meeting (IEDM)*, Dec. 2012, pp. 15.2.1–15.2.4.

[22] L. C. Popa and D. Weinstein, "Switchable piezoelectric transduction in AlGaN/GaN MEMS resonators," in *Proc. 17th Int. Conf. Solid-State Sens., Actuators, Microsyst. (TRANSDUCERS EUROSENSORS)*, Jun. 2013, pp. 2461–2464.

[23] A. Ansari and M. Rais-Zadeh, "HEMT-based read-out of a thickness-mode AlGaN/GaN resonator," in *Proc. IEEE Int. Electron Devices Meeting (IEDM)*, Dec. 2013, pp. 18.3.1–18.3.4.

[24] M. Faucher, Y. Cordier, M. Werquin, L. Buchaillot, C. Gaquiere, and D. Theron, "Electromechanical transconductance properties of a GaN MEMS resonator with fully integrated HEMT transducers," *J. Microelectromech. Syst.*, vol. 21, no. 2, pp. 370–378, Apr. 2012.

[25] F. Niebelschütz *et al.*, "AlGaN/GaN-based MEMS with two-dimensional electron gas for novel sensor applications," *Phys. Status Solidi C*, vol. 5, no. 6, pp. 1914–1916, 2008.

[26] B. A. Auld, *Acoustic Fields and Waves in Solids*, vol. 1. Melbourne, FL, USA: Krieger, 1990.

[27] S. Wang, W.-C. Chen, B. Bahr, W. Fang, S.-S. Li, and D. Weinstein, "Temperature coefficient of frequency modeling for CMOS–MEMS bulk mode composite resonator," *IEEE Trans. Ultrason., Ferroelectr., Freq. Control*, in press.

[28] J. D. Joannopoulos, S. G. Johnson, J. N. Winn, and R. D. Meade, *Photonic Crystals: Molding the Flow of Light*, 2nd ed. Princeton, NJ, USA: Princeton Univ. Press, 2011.

[29] C. Kittel, *Introduction to Solid State Physics*. Hoboken, NJ USA: Wiley, 2004.

[30] B. Greene *et al.*, "High performance 32 nm SOI CMOS with high-k/metal gate and 0.149 μm^2 SRAM and ultra low-k back end with eleven levels of copper," in *Proc. Symp. VLSI Technol.*, Jun. 2009, pp. 140–141.
[31] COMSOL, Inc. *COMSOL Multiphysics*. [Online]. Available: http://www.comsol.com, accessed Jan. 2014.
[32] J.-P. Berenger, "A perfectly matched layer for the absorption of electromagnetic waves," *J. Comput. Phys.*, vol. 114, no. 2, pp. 185–200, 1994. [Online]. Available: http://www.sciencedirect.com/science/article/pii/S0021999184711594
[33] S. G. Johnson, M. Ibanescu, M. A. Skorobogatiy, O. Weisberg, J. D. Joannopoulos, and Y. Fink, "Perturbation theory for Maxwell's equations with shifting material boundaries," *Phys. Rev. E*, vol. 65, p. 066611, Jun. 2002. [Online]. Available: http://link.aps.org/doi/10.1103/PhysRevE.65.066611
[34] W. Wang and D. Weinstein, "Acoustic Bragg reflectors for Q-enhancement of unreleased MEMS resonators," in *Proc. Joint Conf. IEEE Int. Freq. Control Eur. Freq. Time Forum (FCS)*, May 2011, pp. 1–6.
[35] J. Tromp, "A coupled local-mode analysis of surface-wave propagation in a laterally heterogeneous waveguide," *Geophys. J. Int.*, vol. 117, no. 1, pp. 153–161, 1994.
[36] S. G. Johnson, P. Bienstman, M. A. Skorobogatiy, M. Ibanescu, E. Lidorikis, and J. D. Joannopoulos, "Adiabatic theorem and continuous coupled-mode theory for efficient taper transitions in photonic crystals," *Phys. Rev. E*, vol. 66, p. 066608, Dec. 2002.
[37] S. G. Johnson *et al.*, "Coupling, scattering, and perturbation theory: Semi-analytical analyses of photonic-crystal waveguides," in *Proc. 5th Int. Conf. Transparent Opt. Netw.*, vol. 1. Jun./Jul. 2003, pp. 103–109.
[38] B. E. Little and H. A. Haus, "A variational coupled-mode theory for periodic waveguides," *IEEE J. Quantum Electron.*, vol. 31, no. 12, pp. 2258–2264, Dec. 1995.
[39] B. Gustavsen and A. Semlyen, "Rational approximation of frequency domain responses by vector fitting," *IEEE Trans. Power Del.*, vol. 14, no. 3, pp. 1052–1061, Jul. 1999.
[40] R. Tabrizian, M. Rais-Zadeh, and F. Ayazi, "Effect of phonon interactions on limiting the $f.Q$ product of micromechanical resonators," in *Proc. Int. Solid-State Sens., Actuators, Microsyst. Conf. (TRANSDUCERS)*, Jun. 2009, pp. 2131–2134.
[41] A. Grill, "Porous pSiCOH ultralow-k dielectrics for chip interconnects prepared by PECVD," *Annu. Rev. Mater. Res.*, vol. 39, no. 1, pp. 49–69, 2009.
[42] G. Degrande, G. De Roeck, P. Van Den Broeck, and D. Smeulders, "Wave propagation in layered dry, saturated and unsaturated poroelastic media," *Int. J. Solids Struct.*, vol. 35, nos. 34–35, pp. 4753–4778, 1998.

Bichoy Bahr (S'10) received the B.Sc. (Hons.) and M.Sc. degrees in electrical engineering from Ain Shams University, Cairo, Egypt, in 2008 and 2012, respectively. He is currently pursuing the Ph.D. degree with the Department of Electrical Engineering, Massachusetts Institute of Technology (MIT), Cambridge, MA, USA. He was an Analog/Mixed Signal and MEMS Modeling/Design Engineer with MEMS Vision, Egypt. He is a Research Assistant with the HybridMEMS Group, MIT. His research interests include the design, fabrication, modeling, and optimization of monolithically integrated unreleased MEMS resonators in standard ICs technology. He is also interested in multiGHz MEMS-based monolithic oscillators, coupled oscillator-arrays, and unconventional signal processing.

Radhika Marathe (S'11) received the B.S. (Hons.) degree in electrical engineering from the California Institute of Technology, Pasadena, CA, in 2009, and the M.S. degree in electrical engineering and computer science from the Massachusetts Institute of Technology, Cambridge, MA, in 2011, where she is currently pursuing the Ph.D. degree with the Department of Electrical Engineering. Her current research interests include the study of hybrid CMOS-MEMS devices and integrated micromechanical resonators for scaling of communication front-end components to multiGHz frequencies.

Dana Weinstein received the B.A. degree in physics and astrophysics from the University of California, Berkeley, in 2004, and the Ph.D. degree in applied physics from Cornell University, in 2009, working on multiGHz MEMS. She is currently an Associate Professor of Electrical Engineering and Computer Science at the Massachusetts Institute of Technology. She is the recipient of the NSF CAREER Award, the DARPA Young Faculty Award, the Intel Early Career Award, and the IEEE IEDM Roger A. Haken Best Paper Award. Her current research focuses on hybrid MEMS-IC devices for low-power wireless communication, microprocessor clocking, and sensing applications. In particular, she is working to harness the benefits of acoustic vibrations to enhance the performance of next-generation electron devices.